January 2005

Metal-Insulator Transition in Doped Single-Wall Carbon Nanotubes

Juraj Vavro
University of Pennsylvania

J. M. Kikkawa
University of Pennsylvania

John E. Fischer
University of Pennsylvania, fischer@seas.upenn.edu

Postprint version. Copyright American Physical Society. Published in *Physical Review B*, Volume 71, Article 155410, 2005, 11 pages.
Publisher URL: http://link.aps.org/abstract/PRB/v71/e155410

Metal-Insulator Transition in Doped Single-Wall Carbon Nanotubes

Abstract
We find strong evidence for a metal-insulator (MI) transition in macroscopic single wall carbon nanotube conductors. This is revealed by systematic measurements of resistivity and transverse magnetoresistance (MR) in the ranges 1.9-300 K and 0-9 Tesla, as a function of p-type redox doping. Strongly H_2SO_4-doped samples exhibit small negative MR, and the resistivity is low and only weakly temperature dependent. Stepwise de-doping by annealing in vacuum induces a MI transition. Critical behavior is observed near the transition, with $\rho(T)$ obeying power-law temperature dependence, $\rho(T) \propto T^{-\beta}$. In the insulating regime (high annealing temperatures) the $\rho(T)$ behavior ranges from Mott-like 3-dimensional (3D) variable-range hopping (VRH), $\rho(T) \propto \exp[(-T_0/T)^{-1/4}]$, to Coulomb-gap (CGVRH) behavior, $\rho(T) \propto \exp[(-T_0/T)^{-1/2}]$. Concurrently, $MR(B)$ becomes positive for large B, exhibiting a minimum at magnetic field B_{min}. The temperature dependence of B_{min} can be characterized by $B_{min}(T) = B_c(1 - T/T_c)$ for a large number of samples prepared by different methods. Below a sample-dependent crossover temperature T_c, $MR(B)$ is positive for all B. The observed changes in transport properties are explained by the effect of doping on semiconducting SWNTs and tube-tube coupling.

Comments
Postprint version. Copyright American Physical Society. Published in *Physical Review B*, Volume 71, Article 155410, 2005, 11 pages.
Publisher URL: http://link.aps.org/abstract/PRB/v71/e155410

Metal-Insulator Transition in Doped Single-Wall Carbon Nanotubes

J. Vavro[a], J. M. Kikkawa[b], and J. E. Fischer[a,*]

[a]*Department of Materials Science and Engineering, University of Pennsylvania, Philadelphia, Pennsylvania 19104-6272*

[b]*Department of Physics and Astronomy, University of Pennsylvania, Philadelphia, Pennsylvania 19104-6396*

(Dated: January 14, 2005)

Abstract

We find strong evidence for a metal-insulator (MI) transition in macroscopic single wall carbon nanotube conductors. This is revealed by systematic measurements of resistivity and transverse magnetoresistance (MR) in the ranges 1.9–300 K and 0–9 Tesla, as a function of p-type redox doping. Strongly H_2SO_4-doped samples exhibit small negative MR, and the resistivity is low and only weakly temperature dependent. Stepwise de-doping by annealing in vacuum induces a MI transition. Critical behavior is observed near the transition, with $\rho(T)$ obeying power-law temperature dependence, $\rho(T) \propto T^{-\beta}$. In the insulating regime (high annealing temperatures) the $\rho(T)$ behavior ranges from Mott-like 3-dimensional (3D) variable-range hopping (VRH), $\rho(T) \propto \exp[(T_0/T)^{-1/4}]$, to Coulomb-gap (CGVRH) behavior, $\rho(T) \propto \exp[(-T_0/T)^{-1/2}]$. Concurrently, $MR(B)$ becomes positive for large B, exhibiting a minimum at magnetic field B_{min}. The temperature dependence of B_{min} can be characterized by $B_{min}(T) = B_c(1 - T/T_c)$ for a large number of samples prepared by different methods. Below a sample-dependent crossover temperature T_c, $MR(B)$ is positive for all B. The observed changes in transport properties are explained by the effect of doping on semiconducting SWNTs and tube-tube coupling.

PACS numbers: 71.23.-k, 71.30.+h, 73.22.-f, 73.63.-b, 73.63.Fg, 75.47.-m, 81.07.-b, 81.07.De

*Electronic mail: fischer@seas.upenn.edu

I. INTRODUCTION

Single-wall carbon nanotubes (SWNT)[1] have attracted considerable interest due to their one-dimensional (1D) character. Bulk SWNT can be viewed as a unique form of granular or nanoporous material composed of 1D objects. This system is inhomogeneous since it contains a random distribution of metallic and semiconducting elements. Studying its transport properties may give information about properties of ropes and tubes, and finding how transport properties depend on the structure of SWNT material can make transport measurements a useful characterization tool. Transport phenomena in bulk SWNT were studied by many authors.[2–7] Results were usually interpreted in terms of Mott-like 3D and 2D VRH or 2D weak localization (WL). Our work suggests that macroscopic samples of SWNT are essentially 3D despite the 1D character of SWNTs and 2D character of the rope lattice. We present a comprehensive study of resistivity vs. temperature and magnetic field for SWNT bulk samples of widely different morphologies as a function of the degree of H_2SO_4 doping. Strong doping produces metallic behavior with finite zero-temperature conductivity and negative magnetoresistance $MR(B) = \rho(T,B)/\rho(T,0) - 1$, indicative of weak disorder. In weakly-doped samples a power-law $\rho(T)$ dependence is observed, as predicted by scaling theory for the critical regime near a MI transition.[8] The samples annealed at 600°C and above are insulating with VRH being the conduction mechanism. We find that the resistivity ratio $\alpha = \rho(1.9\ \mathrm{K})/\rho(40\ \mathrm{K}) \approx 1.5$–$2.0$ serves to demarcate metallic and nonmetallic regimes. Consistent behavior is seen when comparing materials that were H_2SO_4-doped during synthesis and then vacuum annealed at successively higher temperatures to samples that were doped after acid-free assembly.

A MI transition occurs when disorder is strong enough that the Fermi energy E_F lies away from the extended states, and all states within a few k_BT of E_F are localized. This behavior has been observed in many carbonaceous materials. A. W. P. Fung *et al.*[9] induced a MI transition in carbon fibers by controlling the nanopores in the system. High temperature annealing led to partial graphitization, enlargement of graphite platelets and collapse of the interplanar pores. Heat treated carbon fibers exhibit two-dimensional (2D) metallic behavior.[9] The effect of fluorine-intercalation on transport properties of graphite fibers (C_xF) was studied by S. L. di Vittorio,[10,11] who found that increasing fluorine concentration causes a transition from metallic ($x > 3.6$) to insulating ($x < 3.0$) regime. A MI transition

was observed also in conducting polymer systems, *e.g.* MI transition in ion implanted *p*-phenylenebenzobisoxale,[12] aging induced MI transition in H_2SO_4 doped polyphenylenevinylene,[13] and disorder-induced MI transition in polyaniline doped with camphor sulfonic acid.[14]

In our experiments a MI transition is initiated by heat treatment of doped samples. At high doping levels, a sufficiently large number of semiconducting nanotubes is conducting and the coupling between nearest-neighbor (NN) nanotubes increases. Consequently, the electron wavefunction $\psi \propto \exp(-\chi r)$ extends over many nanotubes, *i.e.* the effective decay length $1/\chi$ is large. In this low resistivity regime, SWNT transport properties resemble those of doped conjugated polymers. In both cases 3D behavior is observed although the building blocks are of 1D nature. The 1D character of the electronic structure (*i.e.*, the existence of van Hove singularities) and the resulting anisotropy was probed in both metallic and insulating regimes of partially aligned fibers by polarized Raman spectroscopy.[15]

For undoped samples, the charge carriers are localized predominantly on metallic nanotubes, and the typical energy separation between NN localized states Δ_ξ depends on the dimensionality of the wave function, the localization length ξ, and the density of states at the Fermi energy, $N(E_F)$. In the case of short tubes and weak tube-tube coupling, another important energy scale is the Coulomb charging energy, E_c, similar to the case of granular and porous carbon structures.[9,16] We observed CGVRH conductivity at low temperature for HiPco samples annealed at 1150°C.

II. SAMPLE DESCRIPTIONS

All samples have been exposed to air and are thus presumably p-doped to some extent by atmospheric oxygen.[17–19] We will use the term 'undoped' in the sense 'air exposed but otherwise undoped'.

Samples include 1) partially-aligned fibers HPR[15] made from purified HiPco[20] SWNT; 2) buckypaper PLV-H of pulsed laser vaporization[21] (PLV) SWNT aligned in 26 T magnetic field;[22,23] 3) buckypaper PLV of random PLV SWNT and 4) buckypaper HPG of random HiPco SWNT. Groups 1) and 2) are from R. E. Smalley's group at Rice University; 3) is synthesized by H. Kataura at Tokyo Metropolitan University,[24] and 4) is from T. V. Sreekumar at Georgia Institute of Technology.[25]

HPR fiber has been extruded from nanotubes suspended in oleum (100% sulfuric acid

saturated with SO_3 to eliminate trace water). Consequently, as-received air-exposed fiber is strongly acid-doped, confirmed by thermopower[26] and Raman measurements,[15] and referred to as HPR Neat. The fibers exhibit axial preferred orientation with mosaic full width at half-maximum (FWHM) 44°.[15] To study the effect of different doping levels, samples of neat fibers are annealed in vacuum at 300, 600, 900 and 1150°C. We refer to these as HPR T300, T600, T900 and T1150. Annealing at 1150°C leads to 34–38% weight loss, equivalent to 21-24 carbons per acid formula unit in HPR Neat.

As-received PLV buckypaper is undoped, and is doped by immersion in 95% H_2SO_4 or 70% HNO_3, or by exposure to Br_2, all for several hours at 295K. Acid doped samples are dried at 100°C in air. Raman scattering,[27] thermopower,[26] resistivity and reflectivity[27] all show that under these conditions H_2SO_4 gives the strongest p-doping effect, compared to HNO_3 and Br_2. The tubes in this material are randomly oriented in the film plane, but they exhibit 62° FWHM out-of-plane preferred orientation as a consequence of filter deposition.[28]

The as-received PLV-H buckypaper is annealed at 1150°C before measurement. We have not performed doping experiments on this material. Out-of-plane preferred orientation from the combined effects of magnetic field and filter deposition is quite pronounced, FWHM = 27°, while the in-plane value characteristic of field alignment alone is 34°.[28]

As-received HPG buckypaper is prepared from oleum suspension similar to HPR fiber, but is washed with acetone in the final preparation step[25] which removes some of the residual acid (henceforth HPG Raw). This is confirmed by the smaller 17% weight loss upon 1150°C vacuum annealing (HPG T1150), corresponding to ~ 40 carbons per acid formula unit in HPG Raw. Doping is restored by immersion of the sample in sulfuric acid (HPG Doped). The out-of-plane FWHM was 44°.[28]

III. EXPERIMENTAL RESULTS AND DISCUSSION

A. Resistivity

Controlling the free carrier concentration by doping and annealing allows us to study the resistivity $\rho(T)$ in metallic, critical and insulating regimes. The temperature dependence $\rho(T)$ for samples with varying doping levels is shown in Fig. 1. Due to the absence of long range order, the temperature coefficient of resistivity (TCR), $\mathrm{d}\rho/\mathrm{d}T$, is negative at

low T for all samples. Strongly doped samples exhibit finite zero-temperature conductivity, $\sigma(T) = \sigma_0 + \Delta\sigma(T)$, indicating metallic transport. Disorder is less important at high temperature, and we observe a positive TCR above 100 K for samples with the lowest resistance. With increasing annealing temperature, the low-temperature upturn in ρ becomes more pronounced; for HPR T1150 and HPG T1150 (samples 1 and 2), $\rho(1.9K)$ increases by more than four decades after annealing at 1150°C. The TCR for these high ρ samples is negative in the whole range 1.9–300 K.

Resistivity results for all 13 samples studied are summarized in Table I and are rank-ordered by decreasing resistivity ratio $\alpha = \rho(1.9\text{ K})/\rho(40\text{ K})$. This parameter serves to classify samples with different microstructures and carrier concentrations, and is a qualitative indicator of the extent of disorder. In the metallic state we find $\alpha \lesssim 1.5$–2. The critical regime is characterized by $2 < \alpha < 4$, and samples with $\alpha > 4$ exhibit VRH transport.

To obtain quantitative insight into $\rho(T)$, the reduced activation energy[14,29]

$$W(T) = -\frac{\mathrm{d}\ln\rho(T)}{\mathrm{d}\ln T} \quad , \tag{1}$$

is also shown (Fig. 2). The low T behavior of W can be used to identify transport regimes.[13] In the metallic regime, $W \approx \Delta\sigma(T)/\sigma_0 \to 0$ as the temperature approaches zero, and the sign of $\mathrm{d}W/\mathrm{d}T$ is opposite to that of TCR. Near the critical regime, W is positive and temperature independent at low T. In the insulating regime with VRH transport, W exhibits a power-law T-dependence.

1. Metallic Regime

The reduced activation energy W of all strongly doped samples (9-13) decreases with decreasing T, shown in Fig. 2. Figure 3 is a linear-linear plot of W vs. T down to 1.4 - 1.8 K for the most conductive samples 11-13 (see lower panel of Fig. 2 and Table I). Confidence in extrapolating to $T = 0$ relies on comparisons of these temperatures ($k_B T_{min} \sim$ 0.15 meV) to energy scales of gapping perturbations. Inter-tube tunnelling[30–33], elastic deformations[33–38] and intrinsic curvature[38,39] can all open gaps smaller than 0.15 meV under some circumstances. But since these gaps all form around the band crossing energy, E_0, the associated insulating behavior would be experimentally unresolved only when $|E_F - E_0| < k_B T_{min}$, which is clearly not the case in our heavily doped samples.[26] In practice, however,

one can never rule out insulating behavior below the temperature floor of the experiment, and lower temperature data is always desirable. Based on the temperature range studied here, the data do extrapolate to $W \lesssim 0$ as $T \to 0$ for samples 12 and 13, and the behavior for samples 9-11 is not as clear-cut. Since we cannot confidently extrapolate a positive zero-temperature value of W for samples 9-11, we proceed by grouping together all samples with $dW/dT < 0$ as 'metallic' to distinguish borderline samples (9-11) from 'critical' samples where W vs. T is nearly constant and W has an unambiguously positive zero temperature limit. We note that samples 9-13 all exhibit sublogarithmic behavior (e.g.-Fig. 10), which is often used to identify metallic behavior, and also satisfy the Mott criterion for minimum metallic conductivity, $\rho(\text{metal}) <\sim 0.005\ \Omega-\text{cm}$.

The low-temperature behavior of the electrical resistivity $\rho(T)$ and of the magnetoresistance $MR(B)$ in the metallic regime can be explained in terms of WL.[40] According to scaling theory,[8] the dimensionless interblock conductance $g \equiv G/(e^2/\pi\hbar)$ scales with the block size, L, for the appropriate range of L. In the WL regime the phase coherence length L_ϕ is smaller than the localization length ξ, and L_ϕ determines the relevant scale for the temperature dependence of g. The macroscopic conductivity can be written as

$$\sigma \cong \frac{e^2}{\pi\hbar}\, g(L) L^{d-2}\big|_{L=L_\phi} \quad , \tag{2}$$

where d is the dimension and

$$\frac{\mathrm{d}\ln g}{\mathrm{d}\ln L} = (d-2) - \frac{C}{g} \quad , \tag{3}$$

C being a constant. Note that Eq. 2 is valid when $L_\phi \lesssim \xi$ and is not valid in the insulating regime where ξ and the phase scattering rate $1/\tau_\phi$ determine the relevant scale for the temperature dependence of g.[8]

WL originates from the quantum interference of time-reversed paths in electron transport. Due to elastic scattering, paths from $\mathbf{r}$ to $\mathbf{r}'$ generally contribute random phases. In the special case of self-crossing paths, however, the closed loop can be circumscribed in opposite directions. Time-reversed paths interfere constructively at $B = 0$,[40] which leads to enhanced backscattering. Inelastic events at finite T in the interfering paths reduce the effect and σ increases with increasing T. This leads to a zero-field temperature dependence in 3D of the form

$$\sigma_{\text{3DWL}} = \sigma_0(1 + (T/T_0)^{s/2}) \quad , \tag{4}$$

where we have taken $\tau_\phi \propto T^{-s}$ and $L_\phi^2 \propto \tau_\phi$. This behavior leads to finite conductivity σ_0 as $T \to 0$, in contrast to 2D and 1D, which is consistent with the observed behavior of our heavily-doped samples.

Despite the aforementioned differences in the limiting behavior of W as $T \to 0$, the inverse of Eq. 4 fits the resistivity data for strongly doped samples 9 and 10 (HPR Neat and HPG Doped, respectively) very well for $T < 40$ K. However, for doped PLV samples 11-13, the addition of a residual resistivity ρ_0 is necessary:

$$\rho(T) = \frac{1}{\sigma_0(1 + (T/T_0)^{s/2})} + \rho_0 \quad . \tag{5}$$

Values of the fit parameters are shown in Table II. The residual resistivity ρ_0 forms a large fraction of the total resistivity of doped PLV samples, but is negligible for HiPco samples. This different behavior is likely due to different microstructures. While the length of nanotubes in PLV samples is of order 10 μm,[41] tubes in our HiPco samples are about 0.5 μm long. Assuming that WL results from NN tunneling, we would conclude that in PLV the intrinsic tube resistance and NN tunneling make comparable contributions to the macroscopic ρ, while in HiPco material NN tunneling is dominant.

2. Critical Regime

A MI transition in 3D is associated with the fact that $\mathrm{d}\ln g/\mathrm{d}\ln L$ vanishes at some $g = g_c$ and can be approximated by

$$\frac{\mathrm{d}\ln g}{\mathrm{d}\ln L} = h\ln(g/g_c) \quad , \tag{6}$$

where h is a constant of order unity.[8] By integrating Eq. 6 one can find

$$g(L) \approx g_c\left(1 + \delta(L/L_0)^h\right) \quad , \tag{7}$$

where $\delta \equiv (\ln g_0 - \ln g_c) \cong (g_0 - g_c)/g_c \ll 1$ is the 'control parameter' and g_0 is the conductance on some microscopic scale L_0. The system remains in the critical regime as long as L is smaller than the correlation length $L_c \propto L_0\delta^{-1/h}$. For $L \gg L_c$ the system is metallic if $g_0 > g_c$, and Eqs. 3 and 4 apply. If $g_0 < g_c$ the system is insulating for $L \gg L_c$, $g \propto \exp(-L/L_c)$, and the physical meaning of L_c in the insulating phase is the localization length ξ.[8]

In the critical regime $g \approx g_c$ and according to Eq. 2 the large-sample resistivity follows a power law behavior[8]

$$\rho(T) = aT^{-\beta} \quad . \tag{8}$$

This behavior leads to constant reduced activation energy $W(T) = \beta$, as is the case for low T behavior of HPR T300 and HPG Raw (samples 7 and 8), shown in Fig. 2.

The power-law dependence of $\rho(T)$ is universal and requires only that the disordered system be close to a MI transition, *i.e.* in the critical region where $\delta \ll 1$.[14] We obtain good fits to Eq. 8 below 40 K for both samples in the critical regime with $\beta = 0.38$ and 0.31, in agreement with the theoretical prediction $1/3 \lesssim \beta \lesssim 1$.[14,42] The resistivity ratios α for these samples are $2 \lesssim \alpha \lesssim 4$, shown in Table I.

3. Insulating Regime

When doping is sufficiently weak to reduce the tube-tube coupling, the charge carriers at the Fermi energy become strongly localized, $\xi \ll L_\phi$, and hops with $R > \xi$ are favorable. The low-temperature transport in the insulating regime is by variable-range hopping (VRH)

$$\rho(T) = \rho_0 \exp\left((T_0/T)^p\right) \quad , \tag{9}$$

where $k_B T_0 = 2^{1/p}\Delta_\xi / 2p(1-p)$, Δ_ξ is a characteristic energy separation between NN states, and an average energy needed to make a hop of length r is equal to $\Delta_\xi \cdot (\xi/r)^{\frac{1-p}{p}}$. For d-dimensional Mott[43] VRH, $p = 1/(d+1)$, and for Coulomb-gap[44] (CG) VRH, $p = 1/2$.

To extract the exponent p in Eq. 9, we calculate $W(T)$ and plot it against $\log T$ (Fig. 2). This procedure yields values of p which vary from sample to sample and with annealing temperature. For moderately resistive samples we obtain $p = 0.25 - 0.26$, consistent with 3D VRH ($p = 1/4$). With increasing resistivity we observe increasing p.

For the most resistive samples HPR T1150 and HPG T1150 (1 and 2, respectlively), $\log W(T)$ vs $\log T$ changes slope from $p < 0.4$ to $p = 0.5$ with $k_B T_0 \approx 5.2$ meV. This behavior is similar to crossover from 3D VRH to CG VRH observed in various materials.[45–47] Note that the characteristic energy corresponding to $k_B T_0$, $\Delta_\xi \approx 7.6 k_B$, agrees with the temperature at which the change of VRH behavior takes place.

Both Mott-like VRH (1D) and CG VRH are consistent with $p = 0.5$. 1D VRH is unlikely since the corresponding fit value $T_0 \approx 60$ K would imply $\xi \approx 350$ nm if $N(E_F)$ along the

nanotube axis is 2.187 $\mathrm{eV}^{-1}\mathrm{nm}^{-1}$.[48] The tube length in HPR and HPG samples is $\sim$ 500 nm, not much longer than the inferred ξ so that 1D hopping effects would seem unlikely.

The observed VRH exponent $p \approx 1/3$ in some of our samples is consistent with 2D VRH. However, there is no physical explanation for 2D localization and hopping in our samples, and we rather interpret this value of VRH exponent as a transition between Mott-like 3D VRH ($p = 1/4$) and CG VRH ($p = 1/2$).

Coulomb interactions and the charging energy E_c in granular systems open a Coulomb gap $\Delta_c \propto N_0(E_F)^{1/2}$ at E_F with vanishing density of states at the Fermi level, $N(E) \propto (E-E_F)^2$. The quadratic behavior is universal and does not depend on the unperturbed density of states $N_0(E)$.[44] $\rho(T)$ follows the VRH form, with $p = 1/2$ and

$$k_B T_0 = \frac{2.8e^2}{\kappa\xi} \quad , \tag{10}$$

where κ is the effective dielectric constant. It has been pointed out that in granular systems ξ in Eq. 10 has to be replaced with an effective decay length $1/\chi$.[9,16] Here, the decay occurs over metallic and semiconducting nanotubes, and in the intervening gaps between nanotubes, and is characterized by barrier heights Φ_m, Φ_s and Φ_g, respectively. The effective reciprocal decay length χ is calculated as a weighted average of reciprocal lengths over tubes and gaps:

$$\chi = \frac{r_m}{r}\chi_m + \frac{r_s}{r}\chi_s + \frac{r_g}{r}\chi_g \quad , \tag{11}$$

where $r = r_m + r_s + r_g$ is the hopping distance and r_i, $i = m, s, g$, is the total span of region i (m = metallic tube, s = semiconducting tube, g = gap between nanotubes).

Although the wave-function decay within the nanotube can be small, NN hopping is not necessarily more likely than VRH due to the fluctuations in the nanotube energy. The fluctuations make NN hops energetically less favorable then distant hops[16] and, provided that χ is small due to large energy fluctuations, the hopping distance $R \sim \chi^{-1}\sqrt{T_0/T}$ can be quite long. Φ_m and Φ_s exist due to nanotube energy fluctuations, of which there are two types.[16] The first is due to random disorder potential in the surroundings of each nanotube (of length L_n). This fluctuating potential changes the charging energy $E_c \propto 1/L_n$ by an amount not exceeding the original value, since discharge to the ground state would result in an even larger change in E_c.[16,49] The perturbed energy is then distributed within the range $E_F \pm 2E_c$.[49] The second type arises from quantum size effects which cause an energy splitting $E_q \propto 1/L_n$ within an individual nanotube. Note that both E_c and E_q are

inversely proportional to tube length. This explains why we do not observe CG VRH in undoped/annealed PLV SWNT samples since they consist of long tubes.

The effective barrier height for metallic SWNTs is comparable to the fluctuations,[16] $\Phi_m \simeq 2E_c + E_q$. For semiconducting tubes, the position of the Fermi energy with respect to the bottom/top of conduction/valence band has to be taken into account.

The CG VRH mechanism was reported in random SWNT/polymer composites by J. M. Benoit and coworkers.[50] In their experiment, processing designed to isolate tubes in the polymer matrix resulted in only weakly screened Coulomb interactions. In the present work, we achieve an increase of charging energy by annealing, which makes the semiconducting nanotubes very poor conductors. This results in weak g between metallic tubes, and reduced mutual screening. Combining these effects with short tube lengths ($L_n \sim 0.5$ μm) leads to CG VRH at low T.

B. Magnetoresistance

The temperature and field dependence of MR depends on the transport regime. MR is sensitive to disorder and electron interactions[40] and, unlike resistivity, can provide not only temperature dependence of relevant scattering mechnisms but also the corresponding length scales. The sign of MR as a function of doping and/or annealing temperature can provide an indicator for electronic MI transition.[9] More specifically, by extrapolating low T data we are able to determine the sign of the quadratic coefficient of magnetoresistance (QCMR), $\mathrm{d}MR^2/\mathrm{d}B^2|_{B=0}$, at zero temperature. Our data associate a negative sign with the metallic regime, and a positive sign with the nonmetallic regime.

A sampling of the MR data is shown in Figs. 4 and 5. Above 10 K all samples exhibit negative $MR(B)$ which decreases monotonically with B. Below 10 K the magnitude and B dependence are qualitatively different for different resistivity ratios α. In the metallic regime ($\alpha < 2$), MR is negative down to the lowest accessible temperature (Fig. 4b) and the low field behavior is consistent with WL. Samples with diverging low-temperature resistivity ($\alpha > 2$) acquire a positive contribution to $MR(B)$ at higher fields (Figs. 4a and 5). The magnitude of this contribution increases with decreasing T, so $MR(B)$ has a minimum at a temperature- and sample-dependent field B_{min}. Samples with the highest α exhibit positive QCMR at accessible temperatures, Fig. 5a.

1. *Weak Localization*

The negative *MR* in the metallic regime is quadratic at low B, flattening out at higher B. With decreasing temperature, the loss of purely quadratic behavior occurs at lower B. This is consistent with WL theory, which predicts negative *MR* in weakly disordered systems and quadratic behavior below the inelastic-scattering equivalent magnetic field B_ϕ. Time-reversal symmetry is not obeyed in finite magnetic field, which leads to dephasing of the interference between two opposing paths around the loop of self-crossing paths, and to negative *MR*. B_ϕ is equivalent to the field which induces a magnetic flux $A_\phi B_\phi$ of order one flux quantum $\Phi_0 = h/e$ through the area $A_\phi \propto L_\phi^2$ of the interfering loop. B_ϕ is often expressed in the form $B_\phi = \Phi_0/4\pi L_\phi^2$. Since $L_\phi \propto T^{-s/2}$, B_ϕ increases with increasing temperature.

In WL theory *MR* can be expressed in the form $Af(B/B_\phi)$, assuming only one relevant phase-scattering mechanism. This property can be readily tested by scaling; for a given sample we select one *MR* data set at some temperature T_0 and consider this to be $f(B)$. Then we fit $MR(B)$ data at different T to $Af(B/B_\phi)$ with A and B_ϕ as free parameters. This procedure yields the T dependence of (normalized) proportionality constant A and (normalized) phase-scattering equivalent magnetic field B_ϕ. The absolute values of these parameters and the analytical form of $f(x)$ remain undetermined.

We find that the *MR* is scalable in the range 0–9 T but only for metallic samples where *MR* is monotonically negative. Below the temperature at which $MR(B)$ develops a minimum, $MR(B)$ can no longer be expressed as $Af(B/B_\phi)$, *i.e.* in the non-monotonic cases there is clearly more than one scattering mechanism or contribution to *MR*.

Fig. 6 shows the scaling results as the temperature dependence of B_ϕ/B_0 and A/A_0 for metallic samples 9,10,12 and 13. HPR Neat and PLV+H_2SO_4, which show monotonic $MR(B)$ down to 1.9 K, can be fit with a power-law

$$B_\phi \propto T^s \quad , \tag{12}$$

with $s \approx 0.66$. For the other two metallic samples, B_ϕ deviates from power-law T dependence above 7 K; fits to the low T data yield $s \approx 0.77$. Note that in the case of diffusion transport $L_\phi^2 \propto \tau_\phi$, both perpendicular and parallel to the rope axis, and the temperature dependence of B_ϕ is identical to that of the phase scattering rate, $B_\phi \propto 1/\tau_\phi$. As a result, the exponent

s in Eq. 12 should be identical with the exponent s in Eq. 4 and 5. However, only for doped HiPco samples (fit to Eq. 4) are values of s close to those obtained from magnetoresistance data. In the case of doped PLV samples (fit to Eq. 5) there is a large difference between the two values, and the resistivity saturates to a constant value at low T much faster than predicted from MR data.

The T-dependence of the negative second derivative of $MR(B)$ at zero field, $K_\phi \equiv -\mathrm{d}^2 MR/\mathrm{d}B^2|_{B=0}$, is shown in Fig. 7. In both insulating and metallic regimes, the low-field MR is quadratic as shown in Fig 8 for sample 5. For samples in the metallic regime $K_\phi(T)$ approaches power law behavior at low T.

$$K_\phi(T) \propto T^{-\gamma} \quad , \tag{13}$$

with exponent $\gamma \approx 1.0 - 1.2$; these are collected in Table III.

The low T behavior of B_ϕ and K_ϕ of samples in the metallic regime ($\alpha < 2$) qualitatively follow predictions of 3D WL which were used to analyze $\rho(T)$ (Table II). In 3D the WL contribution to magnetoconductivity can be written in the form

$$\Delta\sigma_{\mathrm{3DWL}}(B)/\sigma = A \left(\frac{B}{B_\phi}\right)^{1/2} f_3\left(\frac{B}{B_\phi}\right) \quad , \tag{14}$$

where $A = k_1\sqrt{B_\phi}$, k_1 is a positive constant coefficient, and $f_3(x)$ is the function given by A. Kawabata,[51] who found that $f_3(x)$ goes as $x^{3/2}$ for $x \ll 1$ and is constant for $x \gg 1$. Applying Eq. 14 to calculate $K_\phi(T)$, we get $K_\phi \propto B_\phi^{-3/2}$. Comparing γ from Eq. 13 with exponent s from Eq. 12 we see that in the 3D WL regime $\gamma = 1.5s$. Experimentally obtained values of s and γ, shown in Table III, agree approximately with this relation.

Although our low-field MR data follow Kawabata's 3D WL model quite well, we do not obtain good fits to Eq. 14 at higher fields, *i.e.* the function $f(x)$ we use in the scaling differs from $\sqrt{x}f_3(x)$ for large x. Eq. 14 predicts $\sqrt{B}$ behavior for $B \gg B_\phi$, but the observed dependence is closer to $\ln B$, similar to 2D WL.[52,53] Possible explanations for this discrepancy include contributions to the MR from carrier-carrier interactions and/or anisotropic microstructure resulting from the 1D nature of SWNT. More detailed theoretical analysis is needed to resolve this issue.

We use Eq. 14 and low-field MR data to estimate $L_\phi^2 = \Phi_0/4\pi B_\phi$. For $T = 1.9$ K we obtain L_ϕ^2 approximately 1000 nm^2; a summary of the results is given in Table III. We calculate L_ϕ^2 instead of L_ϕ because SWNT ropes are anisotropic and we expect different diffusion

coefficients for propagation along ($D_\parallel$) and perpendicular to the rope axis ($D_\perp$). For the phase coherence length along and normal to the rope axis we can write $\ell_\parallel^2 \propto \sqrt{D_\parallel/D_\perp} L_\phi^2$ and $\ell_\perp^2 \propto \sqrt{D_\perp/D_\parallel} L_\phi^2$, respectively. This can lead to long $\ell_\parallel$ even for relatively small L_ϕ^2.

The value of L_ϕ can serve as a lower limit for $\ell_\parallel$ and an upper limit for $\ell_\perp$. At 1.9 K we obtain $L_\phi \approx 30$ nm for HiPco samples and $L_\phi \approx 45$ nm for PLV samples. Since bundle diameters in our samples are about 40–70 nm and $\ell_\perp < L_\phi$, the bundles can be considered as anisotropic 3D objects in the whole temperature range 1.9–300 K.

Both transverse *MR* and L_ϕ^2 will depend on the degree of alignment of the anisotropic ropes [28]; only the normal component of the the area $A_\phi \propto L_\phi^2$ of the interfering loop contributes to *MR*. Experiments by McIntosh *et al.*[54] on an individual rope indeed show that the *MR* amplitude decreases as the field direction is varied from perpendicular to parallel with respect to the rope axis. We expect a similar effect to occur in partially aligned bulk SWNT samples such as our films and fibers [28], and *MR* vs. field direction should correlate with degree of alignment.

2. B_{min} vs. T and the MI Transition

In Fig. 9 we plot B_{min} versus T for the subset of HiPco samples exhibiting non-monotonic $MR(B)$. We find $B_{min}(T)$ remarkably linear, $B_{min} = B_c(1 - T/T_c)$ (true as well for PLV samples, not shown). T_c is of particular interest; it is the crossover temperature below which *MR* has positive QCMR. The extrapolated sign of QCMR at $T = 0$ K, which is the same as the sign of T_c, depends on doping/annealing and provides a sensitive indicator for electronic MI transition.[9] We find negative zero-temperature QCMR and T_c for all samples in the metallic regime ($\alpha < 2$). Positive T_c is obtained for nonmetallic samples ($\alpha > 2$).

The linear behavior of $B_{min}(T)$ for all samples is unexpected. One would assume that the negative and positive contributions to *MR* represent two distinct phenomena. For example, if one wishes to explain the positive upturn in $MR(B)$ as a sum of WL (negative) and some other positive contribution, then both must have a common parameter or their parameters have to correlate to ensure linearity of $B_{min}(T)$ for all combinations of the two (*i.e.*, for all samples). Extrapolating the linear fits of $B_{min}(T)$ also reveals that for HiPco-based samples (HPR, HPG), all lines intersect at roughly the same point (-0.3 K, -2.7 T). Three datasets of B_{min} vs. T for PLV-derived samples (PLV Undoped, PLV+Br_2, PLV-H) do not have this

property, perhaps due to their different microscopic properties.

The correlation between T_c (derived from MR) and α (derived from ρ) is shown in Fig. 10b. The most complete data were obtained for HPR fibers; these show convincingly that the crossover temperature T_c decreases slowly with decreasing α in the nonmetallic regime (large α) and then faster as the metallic regime is approached. Samples in the metallic regime have either negative T_c or monotonic $MR(B)$ down to the lowest accessible temperatures. Both $\rho(T)$ and $MR(B)$ give similar α values which demarcate metallic and nonmetallic samples. From the normalized resistivity $\rho_r(T) = \rho(T)/\rho(40\ \mathrm{K})$ versus T shown in Fig. 10a, we estimate that on the metallic side $\alpha < \alpha_c = 1.5$. Since the plot is log-linear, the dotted line represents logarithmic behavior - all $\rho_r(T)$'s above the line have nonmetallic (divergent or superlogarithmic) temperature dependence while all $\rho_r(T)$'s below the line have metallic (nondivergent or sublogarithmic) temperature dependence with finite conductivity at $T = 0$. The observed value of α_c is consistent with the value at which the sign of T_c and QCMR changes from negative to positive, as shown in Fig 10b.

3. Strong Localization

With increasing resistivity ratio α, all samples acquire an increasing positive contribution to MR. One possible origin is the field dependence of carrier-carrier scattering. This correction is large only when the splitting between spin-up and spin-down bands is much greater than the thermal energy k_BT.[11,40] Therefore, the MR associated with carrier-carrier interaction is a high field effect, consistent with the observed positive upturn in $MR(B)$ at high fields and with the negative sign of B_c/T_c.

The positive $MR(B)$ at very low T for samples dominated by CG VRH can be due to spin polarization or wavefunction shrinkage effects. Both predict quadratic field dependence at low B.[9,56] Spin polarization reduces the hopping probability between two singly-occupied states and between a doubly-occupied and an empty state, and MR saturates at high B.[55] Saturation was not observed in our study, but a trend toward saturation in sample 5 (see data at 2.0 K in Fig. 5b) suggests a higher field study of these samples is worthwhile. Regarding wavefunction shrinkage, a positive MR has been predicted for this mechanism in 2D,[56] and the importance of similar effects in bulk SWNT materials needs closer investigation.

At low fields, VRH can also lead to negative MR.[57,58] The mechanism is similar to WL,

except the magnetic flux is enclosed by a loop formed by the hopping path, and the relevant length scale is hopping distance R instead of L_ϕ. Two calculations predict linear[57] or quadratic[58] magnetic field dependence for low fields. Our *MR* data for insulating samples support the latter, but the temperature dependence does not follow the predicted power law, $T^{-3/(d+1)}$, where d is the dimension.[59] Instead, the low field quadratic curvature is non-monotonic with temperature and changes sign (Fig. 7 inset), so in contrast to a prior study of multiwalled carbon nanotubes,[2] no simple correspondence between the data and these theories can be made here.

In any event, any combination of possible *MR* contributions has to satisfy the condition that at $T > T_c$ the total *MR* exhibits a minimum at $B = B_c(1 - T/T_c)$. This condition imposes an important constraint on the available parameter-space, and may lead to a 'universal' *MR* function for SWNT- based materials.

We do not expect that the observed *MR* behavior originates from orbital magnetism.[60] The field scale for such effects is that which gives a flux quantum Φ_0 through the nanotube cross-section. The mean diameter $d \approx 1.2$–1.4 nm in our samples[15,24,25] leads to a maximum magnetic flux of order $\Phi_0/100$, which is too small to alter the band structure of the nanotubes.

IV. SUMMARY

In this paper we investigate the transition from weak to strong localization as a function of charge transfer doping in bulk SWNT samples of varying microstructure. This is done in two ways: by estimating the resistivity ratio at which the crossover temperature T_c, which characterizes the field dependence of the *MR*, changes from positive to negative; and the change from $\rho(T)$ diverging to nondiverging as $T \to 0$. In this manner, both ρ and *MR* data can be interpreted consistently in terms of a MI transition. On the metallic side, the resistivity ratio $\alpha < 1.5$ and low-field *MR* is negative down to the lowest temperatures, with $T^{0.66-0.8}$ temperature dependence of the phase scattering rate $1/\tau_\phi$.

At $\alpha \approx 1.5 - 2$, T_c exhibits an increase from negative to positive while the zero-temperature conductivity changes from finite to zero. In the critical regime $2 < \alpha < 4$, $\rho(T)$ follows a power-law and *MR* is positive at high field. In the insulating regime we observe 3D VRH ($p = 0.25$) for moderately resistive samples. The exponent p increases with

ρ, the most resistive samples exhibiting CG VRH ($p = 0.5$) and positive $MR(B)$ at low T.

We attribute the MI transition to the annealing of doped SWNT samples. Upon dedoping, semiconducting tubes become highly resistive, coupling between metallic tubes weakens and reduced screening leads to stronger Coulomb interactions in the most resistive samples.

An interesting feature of $MR(B)$, and an important result of this experimental study, is the existence of minima at B_{min}, whose temperature dependence is linear *for all measured samples* and regardless of the conduction regime, $B_{min} = B_c(1 - T/T_c)$. This demonstrates that $MR(B)$ cannot be interpreted as an arbitrary linear combination of WL contribution and some positive effect. Instead, the observed behavior suggests that the parameters controlling the behavior of relevant contributions to MR are not independent but they correlate to ensure the linearity of B_{min} vs. T.

T_c is the crossover temperature below which low-field $MR(B)$ has positive zero-field quadratic coefficients. For given sample T_c increases with α. Samples in the metallic regime have negative T_c or their $MR(B)$ is monotonic in the accessible temperature range. Zero T_c was identified with an electronic MI transition.

Acknowledgments

This research was supported by the US Department of Energy, Grant No. DE-FG02-98ER45701 (JV, JEF), and by DARPA under ONR grant N00015-01-1-0831 (JMK). We are grateful to Dr. T. V. Sreekumar, Dr. H. Kataura and Prof. R. E. Smalley for supplying the SWNT samples. We thank E. J. Mele and C. L. Kane for helpful discussions.

---

[1] S. Iijima, Nature **354,** 56 (1991).

[2] Y. Yosida and I. Oguro, J. Appl. Phys. **86,** 999 (1999).

[3] J. E. Fischer, H. Dai, A. Thess, R. Lee, N. M. Hanjani, D. L. Dehaas, and R. E. Smalley, Phys. Rev. B **55,** R4921 (1997).

[4] G. T. Kim, J. G. Park, Y. W. Park, K. Liu, G. Dusberg, and S. Roth, Synt. Met. **103,** 2551 (1999).

[5] G. T. Kim, E. S. Choi, D. C. Kim, D. S. Suh, Y. W. Park, K. Liu, G. Duesberg, and S. Roth, Phys. Rev. B **58,** 16064 (1998).

[6] M. S. Fuhrer, W. Holmes, P. L. Richards, P. Delaney, S. G. Louie, and A. Zettl, Synt. Met. **103,** 2529 (1999).

[7] L. Grigorian, K. A. Williams, S. Fang, G. U. Sumanasekera, A. L. Loper, E. C. Dickey, S. J. Pennycook, and P. C. Eklund, Phys. Rev. Lett. **80,** 5560 (1998).

[8] Y. Imry, *Introduction to Mesoscopic Physics* (Oxford University Press, New York, 1997).

[9] A. W. P. Fung, M. S. Dresselhaus, and M. Endo, Phys. Rev. B **48,** 14953 (1993).

[10] S. L. di Vittorio, M. S. Dresselhaus, M. Endo, and T. Nakajima, Phys. Rev. B **43,** 12304 (1991).

[11] S. L. di Vittorio, M. S. Dresselhaus, M. Endo, and T. Nakajima, Phys. Rev. B **43,** 1313 (1991).

[12] G. Du, A. Burns, V. N. Prigodin, C. S. Wang, J. Joo, and A. J. Epstein, Phys. Rev. B **61,** 10142 (2000).

[13] M. Ahlskog, R. Menon, A. J. Heeger, T. Noguchi, and T. Ohnishi, Phys. Rev. B **55,** 6777 (1997).

[14] R. Menon, C. O. Yoon, D. Moses, A. J. Heeger, and Y. Cao, Phys. Rev. B **48,** 17685 (1993).

[15] W. Zhou, J. Vavro, C. Guthy, K. I. Winey, J. E. Fischer, L. M. Ericson, S. Ramesh, R. Saini, V. A. Davis, C. Kittrell and M. Pasquali, R. H. Hauge, and R. E. Smalley, J. Appl. Phys. **95,** 649 (2004).

[16] A. W. P. Fung, Z. H. Wang, M. S. Dresselhaus, G. Dresselhaus, R. W. Pekala, and M. Endo, Phys. Rev. B **49,** 17325 (1994).

[17] G. U. Sumanasekera, C. K. W. Adu, S. Fang, and P. C. Eklund, Phys. Rev. Lett. **85,** 1096 (2000).

[18] K. Bradley, S.-H. Jhi, P. G. Collins, J. Hone, M. L. Cohen, S. G. Louie, and A. Zettl, Phys. Rev. Lett. **85,** 4361 (2000).

[19] P. G. Collins, K. Bradley, M. Ishigami, and A. Zettl, Science **287,** 1801 (2000).

[20] I. W. Chiang, B. E. Frinson, A. Y. Huang, P. A. Willis, M. J. Bronikowski, J. L. Margrave, R. E. Smalley, and R. H. Hauge, J. Phys. Chem B **105,** 8297 (2001).

[21] A. Thess, R. Lee, P. Nikolaev, H. Dai, P. Petit, J. Robert, C. Xu, Y. H. Lee, S. G. Kim, A. G. Rinzler, D. T. Colbert, G. E. Scuseria, D. Tománek, J. E. Fischer, and R. E. Smalley, Science **273,** 483 (1996).

[22] J. E. Fischer, W. Zhou, J. Vavro, M. C. Llaguno, C. Guthy, R. Haggenmueller, M. J. Casavant, D. E. Walters, and R. E. Smalley, J. Appl. Phys. **93,** 2157 (2003).

[23] J. Hone, M. C. Llaguno, N. M. Nemes, A. T. Johnson, J. E. Fischer, D. A. Walters, M. J. Casavant, J. Schmidt, and R. E. Smalley, Appl. Phys. Lett. **77,** 666 (2000).

[24] H. Kataura, Y. Maniwa, M. Abe, A. Fujiwara, T. Kodoma, K. Kikuchi, H. Imahori, Y. Misaki, S. Suzuki, and Y. Achiba, Appl. Phys. A: Mater. Sci. Process. **74,** 349 (2002).

[25] T. V. Sreekumar, T. Liu, S. Kumar, L. M. Ericson, R. H. Hauge, and R. E. Smalley, Chem. Mater. **15,** 175 (2003).

[26] J. Vavro, M. C. Llaguno, J. E. Fischer, S. Ramesh, R. K. Saini, L. M. Ericson, V. A. Davis, R. H. Hauge, M. Pasquali, and R. E. Smalley, Phys. Rev. Lett. **90,** 065503 (2003).

[27] J. E. Fischer, W. Zhou, J. Vavro, N. M. Nemes, K. Kamaras (to be published).

[28] W. Zhou, K. I. Winey, J. E. Fischer, S. Kumar, and H. Kataura, Appl. Phys. Lett. **84,** 2172 (2004).

[29] A. G. Zabrodskii and K. N. Zeninova, Sov. Phys. JETP **59,** 425 (1984).

[30] P. Delaney, H. J. Choi, J. Ihm, S. G. Louie, M. L. Cohen, Nature **391** 466 (1998).

[31] P. Delaney, H. J. Choi, J. Ihm, S. G. Louie, M. L. Cohen, Phys. Rev. B **60**, 7899 (1999).

[32] A. Maarouf, C. L. Kane, E. J. Mele, Phys. Rev. B **61**, 11156 (2000).

[33] Y.-G. Yoon, M. S. C. Mazzoni, H. J. Choi, J. Ihm, S. G. Louie, Phys. Rev. Lett. **86**, 688 (2001).

[34] P. E. Lammert, P. Zhang, V.H. Crespi, Phys. Rev. Lett. **84**, 2453 (2000).

[35] T. W. Tombler, C. Zhou, L. Alexseyev, J. Kong, H. Dai, L. Liu, C. S. Jayanthi, M. Tang, S.-Y. Wu, Nature **405** 769 (2000).

[36] J. Cao, Q. Wang, H. Dai, Phys. Rev. Lett. **90**, 157601 (2003).

[37] E. D. Minot, Y. Yaish, V. Sazonova, J.-Y. Park, M. Brink, P. L. McEuen, Phys. Rev. Lett. **90**, 156401 (2003).

[38] C. L. Kane and E. J. Mele, Phys. Rev. Lett. **78**, 1932 (1997).

[39] M. Ouyang, J.-H. Huang, C. L. Cheung, C. M. Lieber, Science **292**, 702 (2001).

[40] P. A. Lee and T. V. Ramakrishnan, Rev. Mod. Phys. **57,** 287 (1985).

[41] J. Liu, A. G. Rinzler , H. Dai, J. H. Hafner, R. K. Bradley, P. J. Boul, A. Lu, T. Iverson, K. Shelimov, C. B. Huffman, F. Rodriguez-Macias, Young-Seok Shon, T. R. Lee, D. T. Colbert, and R. E. Smalley, Science **280,** 1253 (1998).

[42] A. I. Larkin and D. E. Khmelnitskii, Sov. Phys. JETP **56,** 647 (1982).

[43] N. F. Mott and E. A. Davis, *Electronic Processes in Non-Crystalline Materials*, 2nd ed. (Oxford, Clarendon, 1979).

[44] A. L. Efros and B. I. Shklovskii, J. Phys. C **8,** L49 (1975).

[45] Y. Zhang, O. Dai, M. Levy, and M. P. Sarachik, Phys. Rev. Lett. **64,** 2687 (1990).

[46] V. L. Nguyen and R. Rosenbaum, J. Phys.: Condens. Matter **10,** 6083 (1998).

[47] R. Rosenbaum, N. V. Lien, M. R. Graham, and M. Witcomb, J. Phys.: Condens. Matter **9,** 6247 (1997).

[48] R. Saito, G. Dresselhaus, and M. S. Dresselhaus, *Physical Properties of Carbon Nanotubes* (Imperial College Press, 1988).

[49] C. J. Adkins, J. Phys. C **20,** 235 (1987).

[50] J. M. Benoit, B. Corraze, and O. Chauvet, Phys. Rev. B **65,** 241405 (2002).

[51] A. Kawabata, Solid State Commun. **34,** 431 (1980).

[52] B. L. Altshuler, D. E. Khmel'nitskii, A. I. Larkin, and P. A. Lee, Phys. Rev. B **22,** 5142 (1980).

[53] S. Hikami, A. I. Larkin, and Y. Nagaoka, Prog. Theor. Phys. **63,** 707 (1980).

[54] G. C. McIntosh, G. T. Kim, J. G. Park, V. Krstic, M. Burghard, S. H. Jhang, S. W. Lee, S. Roth, and Y. W. Park, Thin Solid Films **417,** 67 (2002).

[55] H. Kamimura and A. Kurobe, Physica B+C **117&118B,** 652 (1983).

[56] B. I. Shklovskii and A. L. Efros, *Electronic Properties of Doped Semiconductors* (Springer-Verlag, Berlin, 1984).

[57] V. L. Nguen, B. Z. Spivak, B. I. Shklovskii, Sov. Phys. JETP **62,** 1021(1985).

[58] U. Sivan, O. Entin-Wohlman, and Y. Imry, Phys. Rev. Lett. **60,** 1566 (1988).

[59] This form of the temperature dependence was given in Ref. [2].

[60] J. P. Lu, Phys. Rev. Lett. **74,** 1123 (1995).

Figures

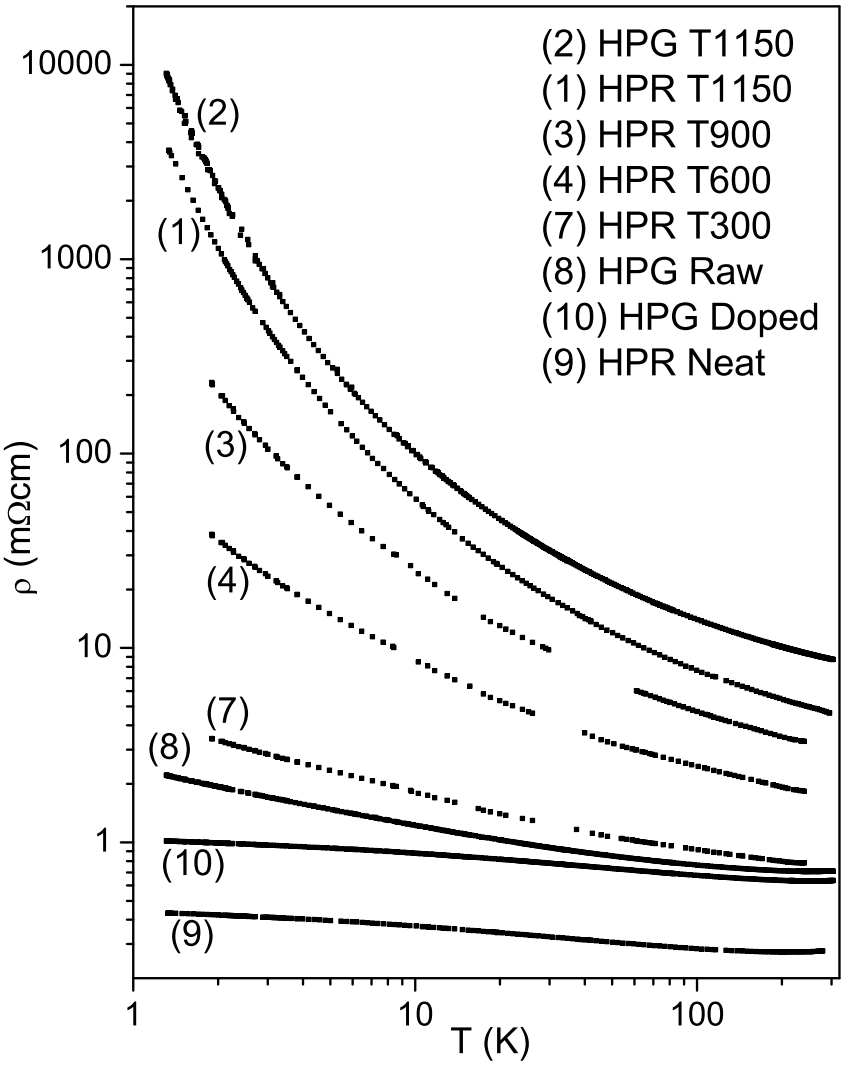

FIG. 1: Resistivity ρ vs. temperature of HPR fibers and HPG buckypaper samples at zero magnetic field. Lightly doped or completely de-doped samples (1-4) show exponential $\rho(T)$ characteristic of variable range hopping, while moderatly doped samples (7, 8) are well represented by a power law divergence (see text). Finally, samples with the highest doping levels of H_2SO_4 (9,10) have small and weakly T-dependent resistivities that satisfy the Mott criterion for minimum metallic conductivity.

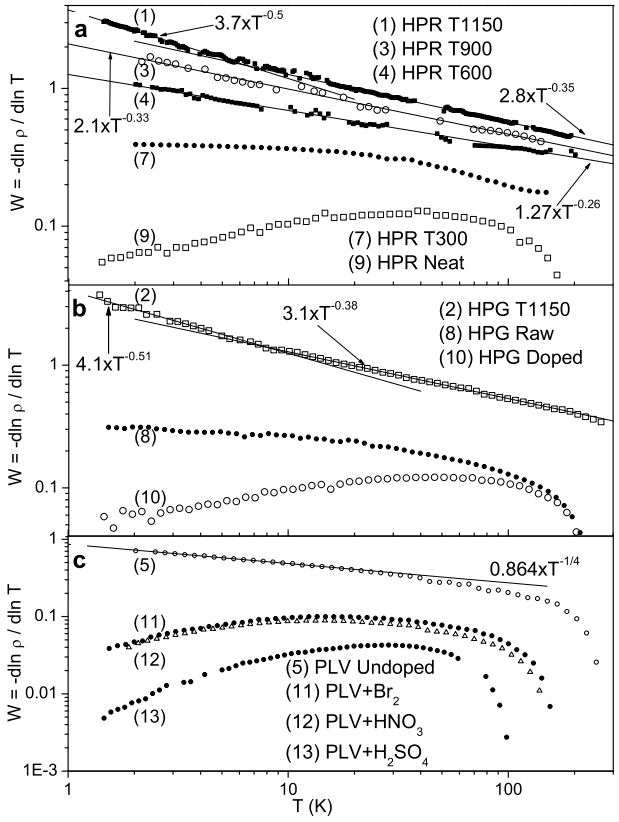

FIG. 2: Reduced activation energy $W = -\mathrm{d}\ln\rho/\mathrm{d}\ln T$ vs temperature for (a) HPR fiber, (b) HPG buckypaper and (c) PLV buckypaper. For metallic samples 9-13, we find $dW/dT < 0$. For samples 7 and 8, $W(T)$ is approximately constant and approaches a finite positive value as $T \to 0$. Finally, insulating samples 1-5 obey $W(T) = p(T_0/T)^p$ (solid lines). The conduction mechanism changes from 3D VRH ($p = 1/4$) to CG VRH ($p = 1/2$) with increasing resistivity.

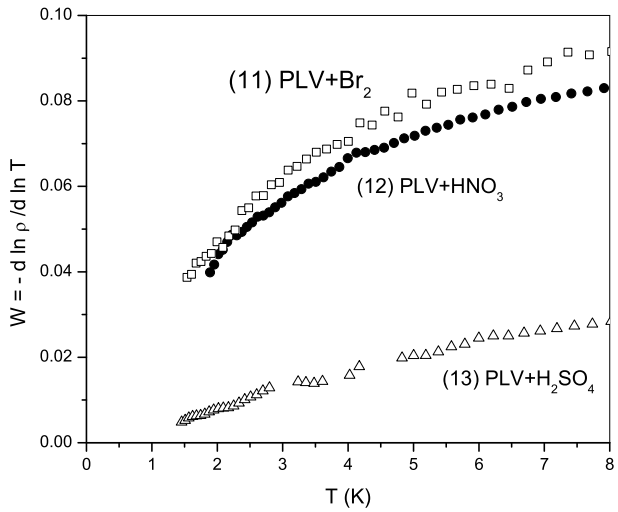

FIG. 3: Linear-linear plots of W vs. T for the PLV samples 11, 12 and 13 doped with bromine, nitric and sulfuric acid, respectively.

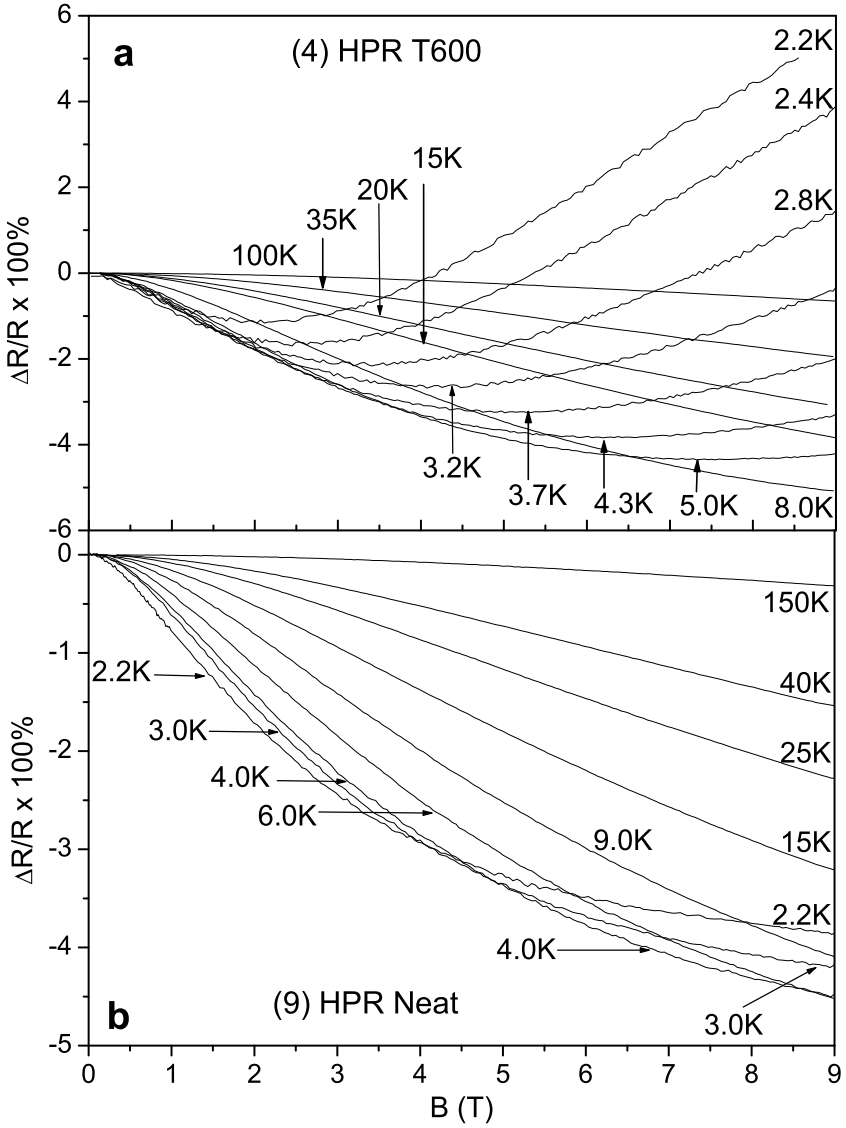

FIG. 4: Transverse magnetoresistance *MR* of (a) HPR fiber annealed at 600°C (sample 4), and (b) strongly doped neat HPR fiber (sample 9). In the doped state *MR* is negative, increasing monotonically in magnitude with increasing field. After annealing *MR* goes through a miminimum and becomes positive at high temperature. In both cases the low field behavior is quadratic.

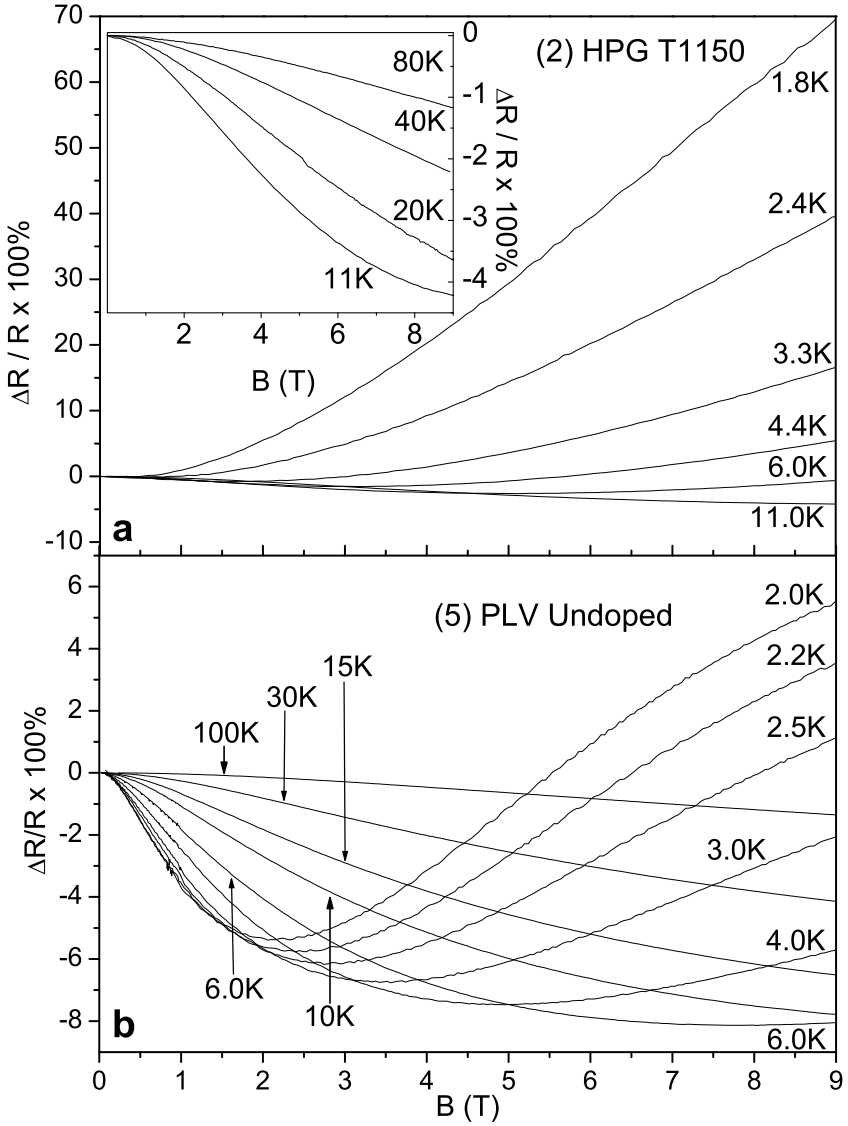

FIG. 5: *MR* of (a) HPG buckypaper annealed at 1150°C (sample 2) and (b) undoped PLV buckypaper (sample 5). At low T, HiPco samples annealed at high temperature exhibit high resistance and positive *MR* with strong temperature dependence at low T. The inset in (a) shows *MR* of annealed HPR fiber above 10 K, which is similar to that of strongly doped samples. *MR* of undoped/annealed PLV samples is similar in magnitude to that in slightly doped HiPco samples.

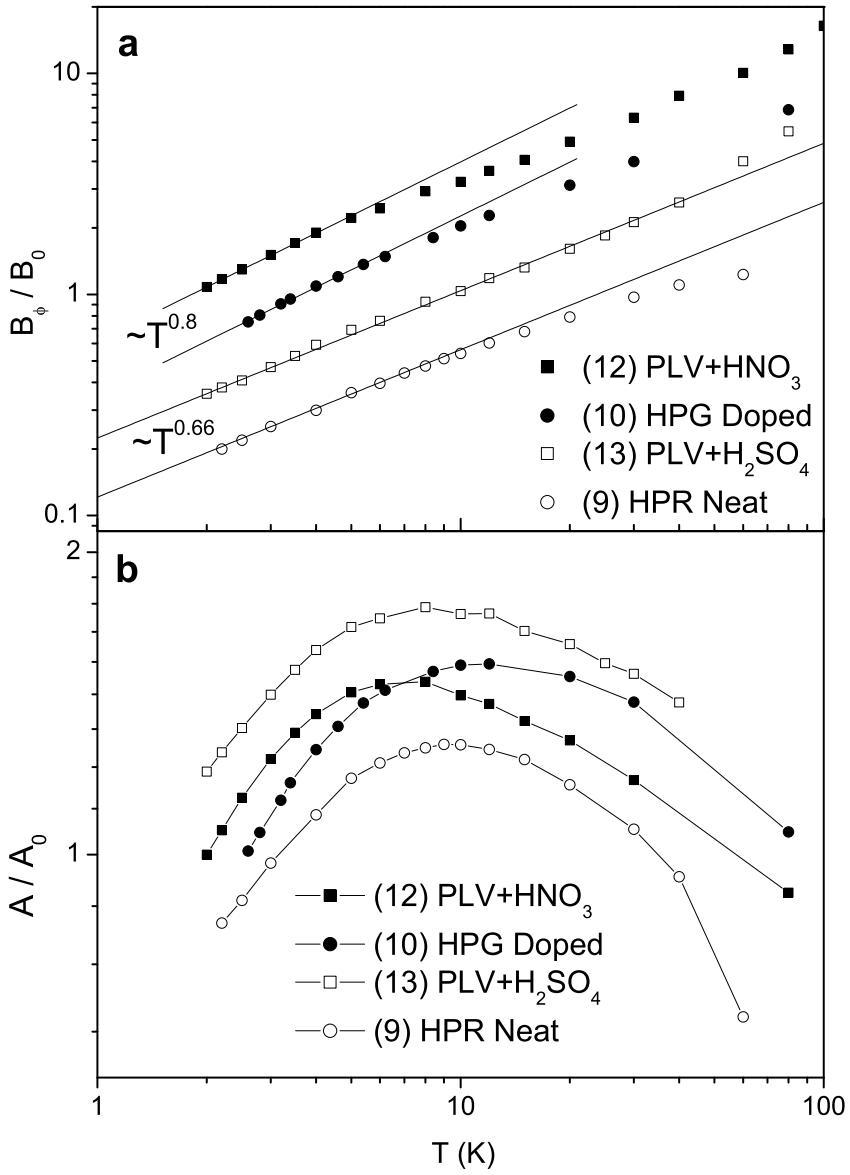

FIG. 6: Analysis of MR data for metallic samples 9,10,12 and 13. (a) Temperature dependence of the weak localization parameter B_ϕ. Good linear fits with $T^{2/3}$ exponents are found for samples with $MR < 0$ at all T (e.g. sample 9, Fig. 4b). (b) Proportionality constant A obtained by scaling MR to $Af(B/B_\phi)$, which suggests that both positive and negative contributions to MR arise from a single mechanism. Lines are guides to the eye. In both figures, normalizations at different temperatures are made to offset the results for clarity.

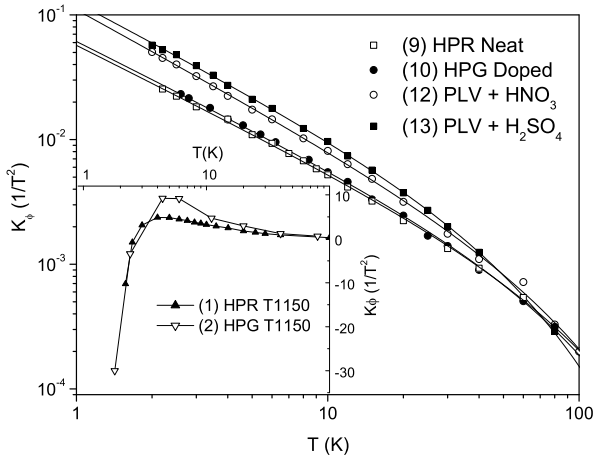

FIG. 7: Temperature dependence of the negative second derivative of $MR(B)$ at zero magnetic field, K_ϕ for metallic samples 9,10,12 and 13. Lines are guides to the eyes. At low T, K_ϕ exhibits power law behavior (Eq. 13) with exponent $\gamma \approx 1.0 - 1.2$ (Table III). Inset shows qualitatively different behavior in the insulating regime, where the sign of $K_\phi(T)$ changes at low temperature (note linear inset y-axis scale) and a positive zero-field magnetoresistance is observed (see text and Fig. 5a).

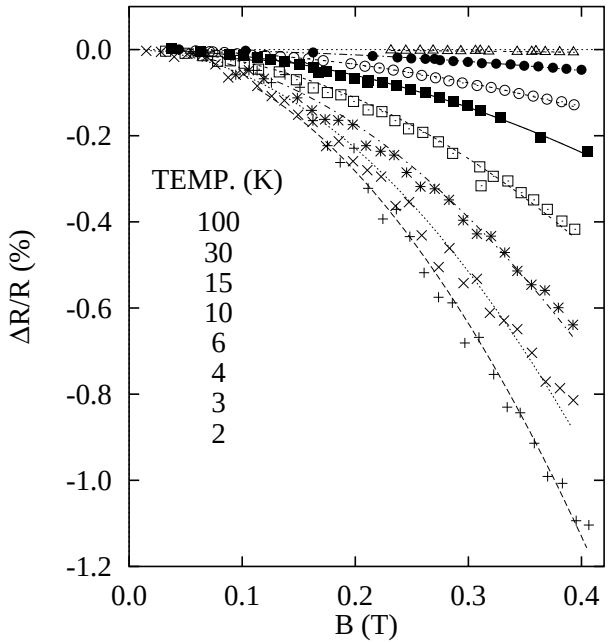

FIG. 8: Low-field $MR(B)$ and quadratic fits for sample 5 from $T = 2$ to 100 K.

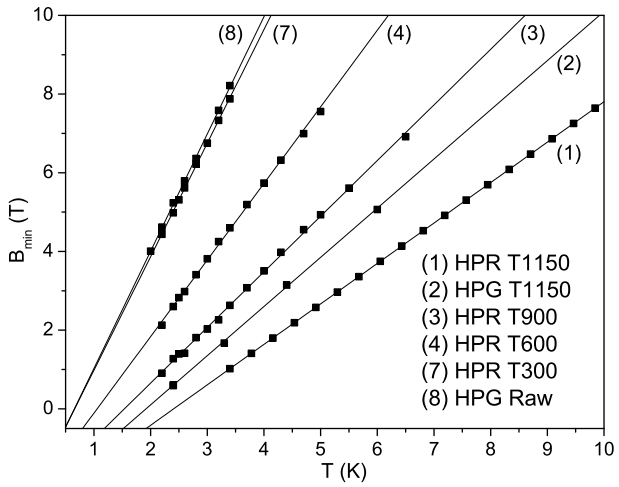

FIG. 9: Magnetic field of the $MR(B)$ minima vs. T for HiPco samples. The fitted linear behaviors all extrapolate approximately to the same point (-0.3 K, -2.7 T).

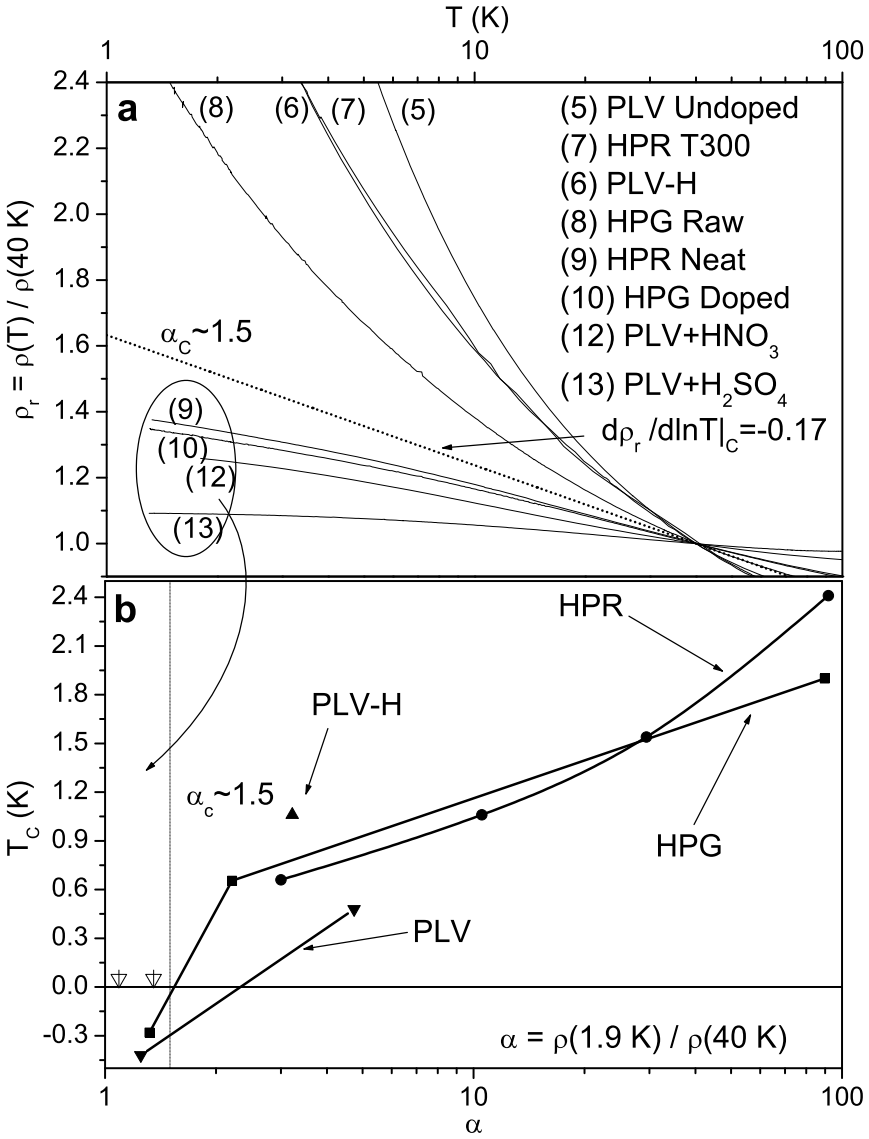

FIG. 10: (a) Temperature dependence of normalized resistivity $\rho_r = \rho(T)/\rho(40\ \mathrm{K})$ for several low-resistivity samples ($\rho_r(1.9\ \mathrm{K}) \equiv \alpha < 5$). Dotted line marks crossover from metallic (sublogarithmic) to nonmetallic (superlogarithmic) behavior and gives estimate for 'critical' resistivity ratio $\alpha_c \approx 1.5$. (b) Plot of crossover temperature T_c ($B_{min}(T_c) = 0$, see Fig. 9) vs resistivity ratio α. The samples exhibiting metallic behavior have either monotonic $MR(B)$ or negative T_c; two short vertical arrows at $T_c = 0$ axis mark α values for samples 9 and 13 with monotonic $MR(B)$ ($\alpha = 1.35$ and 1.09, respectively). Vertical line at $\alpha = \alpha_c$ separates metallic and nonmetallic samples. Lines are guides for eyes.

Tables

TABLE I: Samples used in this study, listed with decreasing values of $\alpha = \rho(1.9\text{ K})/\rho(40\text{ K})$. The table lists zero magnetic field resistivity ρ at $T = 1.9$ K, reduced activation energy W at 1.9 K, resistivity ratio $\alpha = \rho(1.9\text{ K})/\rho(40\text{ K})$ and crossover temperature T_c for all samples studied.

	$\rho(1.9\text{ K})$ (mΩcm)	$W(1.9\text{ K})$	α	T_c (K)
(1) HPR T1150	1300	2.7	91.8	2.41
(2) HPG T1150	2750	2.92	89.8	1.90
(3) HPR T900	225	1.7	29.5	1.54
(4) HPR T600	38	1.08	10.5	1.06
(5) PLV Undoped	55.6	0.74	4.7	0.48
(6) PLV-H	10.1	0.47	3.2	1.06
(7) HPR T300	3.4	0.39	3.1	0.66
(8) HPG Raw	1.97	0.32	2.2	0.66
(9) HPR Neat	0.424	0.061	1.35	—[a]
(10) HPG Doped	0.996	0.057	1.32	-0.28
(11) PLV+Br_2	1.87	0.044	1.29	—[b]
(12) PLV+HNO_3	1.78	0.041	1.25	-0.42
(13) PLV+H_2SO_4	1.01	0.0074	1.09	—[a]

[a] $MR(B)$ vs B monotonic in the accessible temperature range.

[b] MR not measured.

TABLE II: Parameters obtained from fits of resistivity data to a model of 3D weak localization for samples in the metallic regime. Data for HPR Neat and HPG Doped (9 and 10) are fit to Eq. 4 while the doped PLV data (11-13) are fit to Eq. 5.

	σ_0 (Scm^{-1})	T_0 (K)	s	ρ_0 (mΩcm)
(9) HPR Neat	2012	118.9	0.78 ± 0.06	—
(10) HPG Doped	864	155.6	0.72 ± 0.04	—
(11) PLV+Br_2	1393	12.0	1.82 ± 0.08	1.27
(12) PLV+HNO_3	1654	11.1	1.85 ± 0.05	1.27
(13) PLV+H_2SO_4	7362	22.5	2.3 ± 0.10	0.88

TABLE III: Values for the exponent s obtained from scaling of $MR(B)$ data (Eq. 12, Fig. 6), the exponent γ obtained from the fit of $K_\phi(T)$ data (Eq. 13, Fig. 7), and the values of L_ϕ^2 obtained from the fitting of low-field magnetoresistance data to 3D WL model (Eq. 14). (See also Table II.)

	s	γ	L_ϕ^2(1.9 K) (nm^2)	L_ϕ^2(4.0 K) (nm^2)
(9) HPR Neat	0.66 ± 0.03	1.04 ± 0.02	1000	640
(10) HPG Doped	0.77 ± 0.04	1.06 ± 0.02	1000	650
(12) PLV+HNO_3	0.77 ± 0.05	1.16 ± 0.02	1400	900
(13) PLV+H_2SO_4	0.66 ± 0.02	1.12 ± 0.02	1900	1200